

## Article

# On the Wake Properties of Segmented Trailing Edge Extensions

Sidaard Gunasekaran <sup>1</sup>, Daniel Curry <sup>2</sup>

<sup>1</sup> Assistant Professor, Department of Mechanical and Aerospace Engineering, University of Dayton; gunasekarans1@udayton.edu

<sup>2</sup> Undergraduate Student, Department of Mechanical and Aerospace Engineering, University of Dayton; curryd1@udayton.edu

\* Correspondence: gunasekarans1@udayton.edu; Tel.: +1-937-229-5345

**Abstract:** The changes in the amount and the distribution of mean and turbulent quantities in the free shear layer wake of a 2D NACA 0012 airfoil and AR 4 NACA 0012 wing with passive segmented rigid trailing edge (TE) extensions was investigated at the University of Dayton Low Speed Wind Tunnel (UD-LSWT). The TE extensions were intentionally placed at zero degrees with respect to the chord line to study the effects of segmented extensions without changing the effective angle of attack. Force based experiments was used to determine the total lift coefficient variation of the wing with seven segmented trailing edge extensions distributed across the span. The segmented trailing edge extensions had negligible effect of lift coefficient but showed measurable decrement in sectional and total drag coefficient. Investigation of turbulent quantities (obtained through Particle Image Velocimetry (PIV)) such as Reynolds stress, streamwise and transverse RMS in the wake, reveal a significant decrease in magnitude when compared to the baseline. The decrease in the magnitude of turbulent parameters was supported by the changes in coherent structures obtained through two-point correlations. Apart from the reduction in drag, the lower turbulent wake generated by the extensions has implications in reducing structural vibrations and acoustic tones.

**Keywords:** Trailing Edge Extensions; Drag Reduction; Coherent Structures

---

## 1. Introduction

The ideology of application of trailing edge extensions on streamlined bodies to affect wing performance dates to WWII where NACA investigated the use of TE extensions on propeller blades to change the camber and effective angle of attack of propeller sections [1]. Based on the extension geometry, orientation and the airfoil, the design CL can be matched with the operating conditions of the propeller sections to obtain an optimum pressure distribution. Theodorsen and Stickle [1] derived theoretical expressions for the changes in effective angle of attack of the wing as a function of extension length and angle using thin airfoil theory. But validation of theoretical work with experimental work was not done till later. In 1989, Ito [2] performed experimental investigations to study the effect of trailing edge extensions on Göttingen 797 and Wortmann FX 63-137 airfoils used on earlier STOL aircraft, at Reynolds numbers between 300,000 and 1,000,000. The extensions, when placed along the camber-line, significantly increased the CL max and L/D for Gö797 but didn't have any effect on the Wortmann airfoil due to its high camber and a complicated curved lower surface. This result indicated that the effectiveness of the TE extensions depend significantly on the airfoil profile.

This sensitivity on the effectiveness of TE extensions on the airfoil profile is due to angle of the free shear layer wake and characteristic turbulence. Most airfoils experience vortex shedding at the trailing edge resulting in the loss of total pressure, hence drag increase. And similar to a cylinder, the vortex shedding behind a wing is a function of Reynolds number as shown in experiments done by Yarusevych et al [3]. They determined that the roll-up of vortices in the separated shear layer play a key role in the flow transition to turbulence. The effect of vortex shedding on the boundary layer

36 can be seen clearly in Figure 1a and 1b taken from Yarusevych et al. [3] where the smoke released  
 37 downstream of the wing is seen upstream on top of the wing.

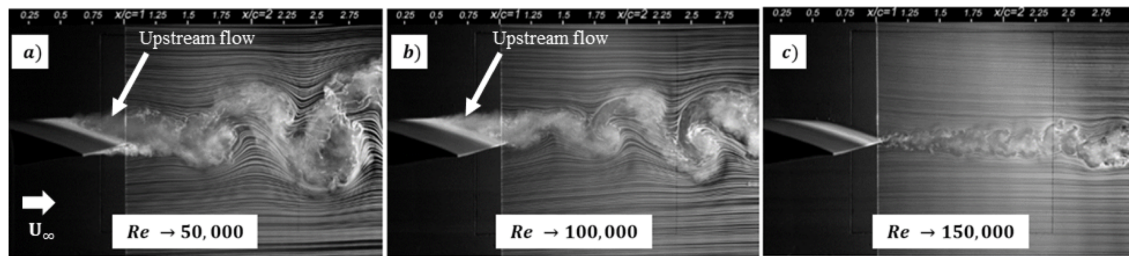


Figure 1. Shedding of vortices from the trailing edge of NACA 0025 airfoil at different Reynolds numbers. [3]

38 Figure 1a and 1b shows prominent turbulent wake vortex shedding due to the separated upper  
 39 surface shear layer. Huang and Lin [4] and Huang and Lee [5] performed experiments on NACA  
 40 0012 airfoil and reported that the vortex shedding is only observed at lower Reynolds numbers where  
 41 boundary layer separation occurs without reattachment. Yarusevych et al. [3] amended this result  
 42 and proved that vortex shedding occurs even after boundary layer attaches to the surface at higher  
 43 Reynolds number as shown in Figure 1c and that the vortex shedding varies linearly with the Reynolds  
 44 number.

45 The vortex shedding is also found to be a function of trailing edge geometry. Guan et al. [6]  
 46 experimented with multiple beveled trailing edge geometries and showed that even subtle changes  
 47 in geometry can result in substantial changes in wake signatures. The vortex shedding was found  
 48 to be greater at the sharp trailing edge when compared to the smooth trailing edges. But even with  
 49 the smooth trailing edge, the turbulent coherent structures were found to convect without distinct  
 50 separation points into the wake which complements the result from Yarusevych et al.[3].

51 Therefore, the effectiveness of the TE extensions depends on the length and angle of the TE  
 52 extension, the airfoil section, the effective angle of attack of the wing, chord based Reynolds number  
 53 and trailing edge geometry. All these parameters affect the vortex shedding behind the wing which  
 54 influences the parasite drag experienced by the wing. The parasite drag contribution on airplanes  
 55 during cruise is in the order of 50% of the total drag [7]. The streamwise pressure gradient created by  
 56 the periodic shedding of vortices initiates on-body flow separation resulting in higher drag, undesirable  
 57 structural vibrations and higher acoustic levels.

58 The current study is aimed at investigating the sensitivity of the segmented TE extensions on  
 59 the amount and distribution of vorticity and the turbulent parameters in the free shear layer wake.  
 60 However, some techniques used to mitigate vortex shedding is shown below.

### 61 1.1. Vortex Mitigation Techniques

62 Most of the parasitic drag reduction methods on a wing is targeted at keeping the boundary layer  
 63 attached and delaying the transition. A slew of active and passive flow control techniques involving  
 64 laminar flow control, wall cooling, hybrid laminar flow control, active wave suppression, use of  
 65 ripples, vortex generators, large eddy breakup devices, surface geometry effects such as streamwise and  
 66 transverse curvatures and microgrooves, synthetic boundary layer, etc were used to prevent boundary  
 67 layer transition and separation. But when compared to the number of methods available to mitigate  
 68 vortex shedding from bluff bodies such as cylinders, trucks, cars, etc. the number of methods available  
 69 to mitigate vortex shedding from streamlined bodies are minimal.

70 One of the popular methods to mitigate the influence of vortex shedding from wing is the use  
 71 of Gurney flaps or divergent trailing edges. Gurney flap is an extension of the trailing edge in the  
 72 direction perpendicular to the chord. The use of Gurney flap generates a favorable streamwise pressure  
 73 gradient at high angle of attack and is known to shift the location of the separation from the leading

74 edge to the quarter chord location while at the same time increasing lift on the main airfoil profile  
 75 (Stanewsky [8]). A finite pressure differential is carried to the trailing edge and is sustained by a vortex  
 76 shedding induced base pressure on the downstream face of the flap. Numerous computational and  
 77 experimental work have been done to study the effect of length and angle of Gurney flaps on vortex  
 78 shedding. (Neuhart and Pendergraft [9], Jang and Ross [10], Storms and Jang [11], Traub [12]). But  
 79 these flaps are usually more effective at higher angles of attack where the flow separates and actually  
 80 generates higher drag as expected in areas where flow is not separated.

81 The disadvantage of higher drag using Gurney flaps at lower angles of attack can be overcome by  
 82 having a static extended trailing edge (SETE) or flexible extended trailing edge (FETE).

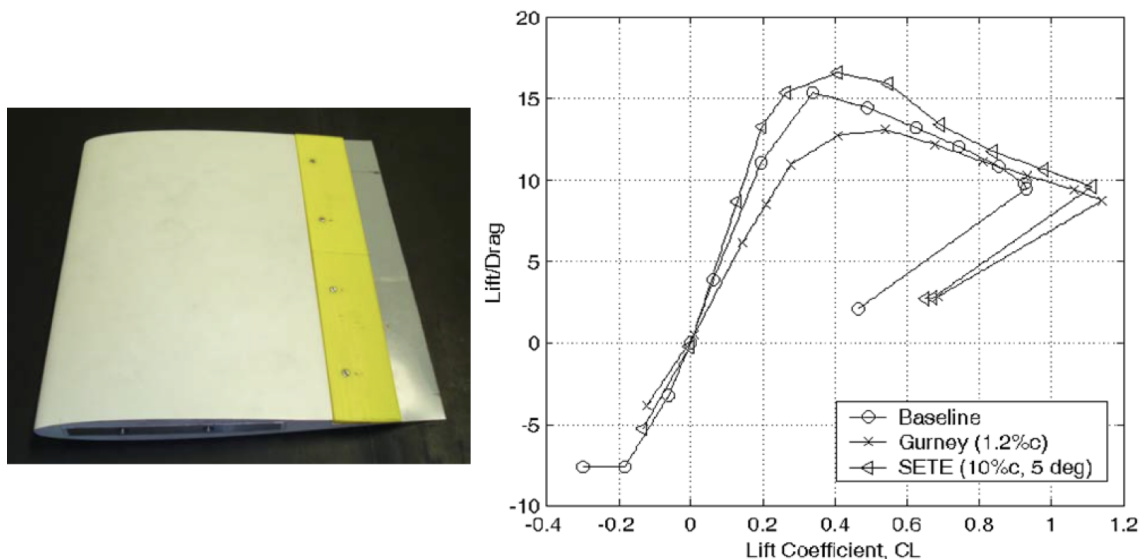
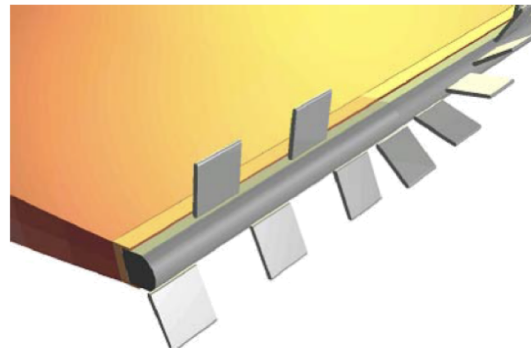


Figure 2. a) NACA 0012 wing with static extended trailing edge. b) Variation of aerodynamic efficiency with coefficient of lift for baseline, Gurney and SETE configurations. The SETE configuration yielded better aerodynamic efficiency than the Gurney flap (Lui et al. [13]).

83 Lui et al. [13] attached a thin flat plate at the trailing edge of NACA 0012 airfoil made of aluminum  
 84 and Mylar and determined the changes in the airfoil efficiency as a function of angle of attack and  
 85 compared it with the measurement made from Gurney flap (Figure 2). SETE showed a larger lift  
 86 increase at a smaller drag penalty better than a Gurney flap since the SETE was in between the wake  
 87 of the main airfoil. SETE shows improvement in lift characteristics across the range of angles of attack  
 88 when compared to Gurney flaps where the lift improvement is seen only at higher angles of attack. Lui  
 89 et al. [13] also determined the aeroelastic deformation for aluminum (less than 1%) and Mylar (13%)  
 90 and postulated that MEMS microphones can be embedded in the SETE which will change and react to  
 91 surroundings. A similar approach is used in this research but instead of using a SETE, a segmented TE  
 92 extensions was used to conserve weight and reduce drag forces on a wing. Segmented TE extensions  
 93 can also act as control surfaces which was implemented by Lee and Kroo [16] where they placed  
 94 microflaps or Miniature Trailing Edge Effectors (MiTE) on the trailing edge of the high aspect ratio  
 95 wings (Figure 3) to suppress flutter through dynamic deflection. With this type of controller, they were  
 96 able to increase the flutter speed by 22%.

97 The background research indicates that extended trailing edges could be effective in reducing  
 98 drag and increasing lift in wings and TE extensions could lead to drag reduction and control flutter  
 99 speed and could possibly act as control surfaces. A major disadvantage of TE extension is that it  
 100 contributes to overall weight of the aircraft. This research explores the use of segmented TE extensions  
 101 as a means to increase the aerodynamic efficiency and reduce the turbulent fluctuations in the wake of  
 102 the wing.



**Figure 3.** Array of MiTEs (Lee and Kroo [14])

**103 2. Experimental Setup**

**104 2.1. Wind Tunnel**

**105** All the experiments were conducted at the University of Dayton Low Speed Wind Tunnel  
**106** (UD-LSWT). The UD-LSWT has a 16:1 contraction ratio, 6 anti-turbulence screens and 4 interchangeable  
**107** 76.2cm x 76.2cm x 243.8cm (30" x 30" x 96") test sections. The test section is convertible from a closed  
**108** jet configuration to an open jet configuration with the freestream range of 6.7m/s (20 ft/s) to 40m/s  
**109** (140 ft/s) at a freestream turbulence intensity below 0.1% measured by hot-wire anemometer. The  
**110** tunnel also has the ability to vary the freestream velocity profile at up to 5 Hz and over 50% velocity  
**111** amplitude using a downstream shuttering system. All the experiments mentioned in the paper were  
**112** done in the open jet configuration where an inlet of 76.2 cm x 76.2 cm opens to a pressure sealed  
**113** plenum. The effective length of the test section in the open jet configuration is 182cm (72"). A 137cm  
**114** x 137cm (44" x 44") collector collects the expanded air on its return to the diffuser. A photo of the  
**115** UD-LSWT open jet configuration is shown in Figure 4. The velocity variation for a given RPM of the  
**116** wind tunnel fan is found using a Pitot tube connected to an Omega differential pressure transducer  
**117** (Range: 0 – 6.9 kPa).

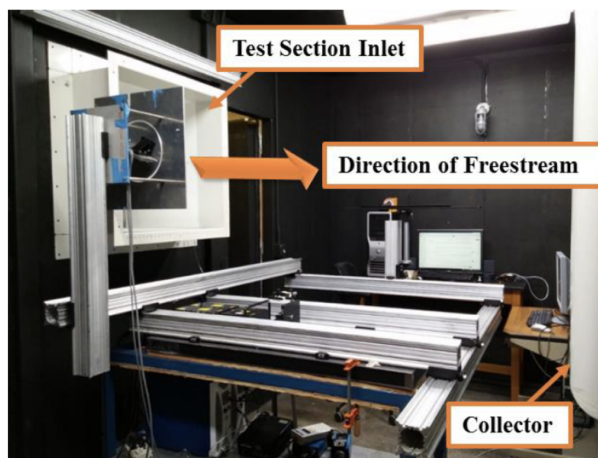


**Figure 4.** University of Dayton Low-Speed Wind Tunnel (UD-LSWT) in the open-jet configuration.

**118 2.2. Test Model**

**119** A NACA 0012 semi-span wing with 20.32 cm span and 10.16 cm chord was designed in SolidWorks  
**120** with capability to attach multiple TE extensions as seen in Figure 5. The wing was then 3D printed  
**121** using Stratasys uPrint SE Plus printer at the University of Dayton. The wing model uses two pieces

122 to clamp the TE extensions to the main wing. The design allows for multiple TE extensions to be  
 123 mounted. Seven segmented plexiglass TE extensions with thickness of 1 mm, length of 2.54 cm ( $l/c =$   
 124 0.25) and a width of 0.635 cm ( $d/c = 0.0625$ ) were used. With the trailing edge extensions, the surface  
 125 area of the wing was increased by 11% when compared to the baseline.

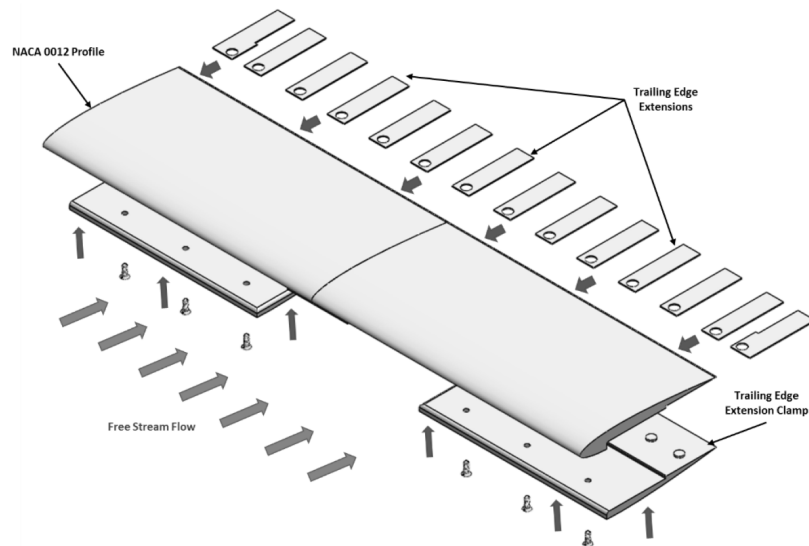


Figure 5. SolidWorks model of AR 4 NACA 0012 wing with TE extensions.

126 *2.3. Force Based Experiment*

127 Force based experiments were performed on the NACA 0012 semispan model with and without  
 128 the segmented TE extensions at a Reynolds number of 200,000 (Test Matrix shown in Table 1). The  
 129 models were tested at an angle of attack range from  $-15^\circ$  to  $+15^\circ$ . Two trials of the same experiment  
 130 were done with increasing and decreasing the angle of attack to check for hysteresis. The schematic of  
 131 the force based test setup is shown in Figure 6.

Table 1. Test Matrix for the force based experiments.

Test Model	Reynolds Number	Angle of Attack (Degrees)
AR 4 NACA 0012 without TE Extensions	200,000	$-15$ to $15$
AR 4 NACA 0012 with TE Extensions	200,000	$-15$ to $15$

132 An ATI Mini-40 force transducer was secured underneath the wing at the quarter chord location  
 133 which interfaced with the Griffin motion rotary stage to change the angle of attack. The rotary stage  
 134 was controlled using the Galil motion software. The schematic of the test setup is shown in Figure 6.  
 135 The root of the wing was made to be in alignment with the splitter plate. The freestream velocity was  
 136 measured using a Pitot tube attached to an Omega differential pressure transducer (Range: 0-6.9 kPa).

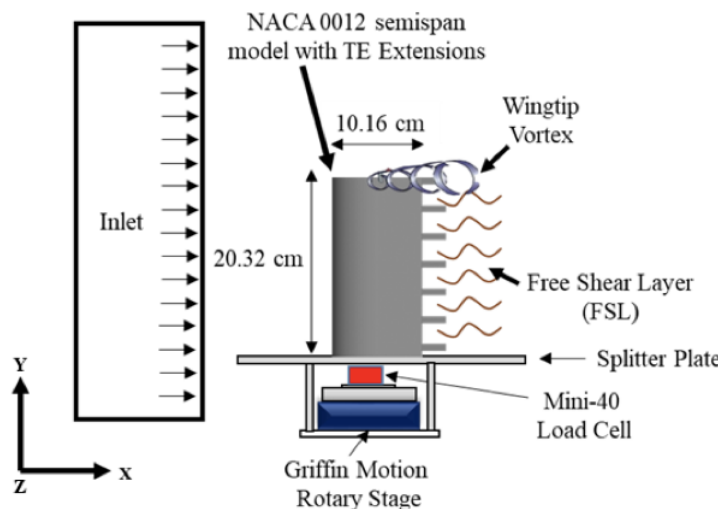


**Figure 6.** Schematic of the force based experiment test setup for NACA 0012 semispan model with TE extensions. Similar setup was used for NACA 0012 wing without TE extensions as well.

#### 137 2.4. Force Transducer

138 An ATI Industrial Automation Mini-40 ([www.ati-ia.com](http://www.ati-ia.com)) sensor was used to determine the wing  
 139 lift and drag coefficients. The specifications for the Mini – 40 sensor are shown in Table 2. The normal  
 140 and axial force was measured using the X and Y axes of the sensor. The sampling rate during data  
 141 acquisition from the Mini-40 was 100 Hz. Tare values were taken before and after each test, and then  
 142 the average of the two tares are subtracted from the normal and axial force readings.

**Table 2.** Test Matrix for the force based experiments.

	$F_X$ (N)	$F_Y$ (N)	$F_Z$ (N)	$T_X$ (Nm)	$T_Y$ (Nm)	$T_Z$ (Nm)
Range	40	40	120	2	2	2
Resolution	1/100	1/100	1/50	1/4000	1/4000	1/4000

#### 143 2.5. PIV Setup

144 Streamwise Particle Image Velocimetry (PIV) was conducted in the free shear layer of the NACA  
 145 0012 wall-to-wall model with and without the segmented TE extensions. Two end plates were installed  
 146 at the wingtips to prevent the rollup of wingtip vortex and reduce three dimensionality. The PIV  
 147 measurements were obtained using a Vicount smoke seeder with glycerin oil and a 200 mJ/pulse Nd:  
 148 YAG frequency doubled laser (Quantel Twins CFR 300). A Cooke Corporation PCO 1600 camera (1600  
 149 x 1200 pixel array) with a 105 mm Nikon lens was used to capture the images. One plano-convex lens  
 150 and one plano-concave lens were used in series to convert the laser beam into a sheet. The laser and the  
 151 camera were triggered simultaneously by a Quantum composer pulse generator. In each test case, over  
 152 1000 image pairs were obtained and processed using ISSI Digital Particle Image Velocimetry (DPIV)  
 153 software. A total of 2 iterations were performed during PIV processing with 64-pixel interrogation  
 154 windows in the first iteration and 32-pixel interrogation windows in the second iteration. Both the  
 155 streamwise and cross-stream PIV interrogations were conducted a Reynolds number of 135,000. The  
 156 test matrix for the PIV experiment is shown in Table 3. The schematic of the PIV test setup is shown  
 157 in Figure 7a. The uncertainty of the velocity measurements from the PIV setup was calculated to be  
 158 0.1 m/s

**Table 3.** Test Matrix for Free Shear Layer (FSL) PIV interrogation

Test Model	Angle of Attack (Degrees)	Interrogation Location
AR 4 NACA 0012 without TE Extensions	0,2,4,6,8	Behind TE
AR 4 NACA 0012 with TE Extensions	0,2,4,6,8	Behind TE Extension

159 In the baseline case, the interrogation window was placed near the trailing edge of the wing as  
 160 shown in Figure 7b to determine the vortex shedding and the momentum deficit. In the wing with  
 161 the segmented TE extensions, the interrogation window was placed at the trailing edge of the TE  
 162 extension as shown in Figure 7a and 7c. Nikon 105 mm lens was used in the streamwise PIV case  
 163 which gave a spatial resolution of 292 pix/cm in both axes. The size of the field of view was 5.5 cm x  
 164 4.1 cm which gave a magnification factor of 0.21. The  $\delta T$  for the images were set to obtain an average  
 165 particle displacement of 8-10 pixels in the wake of the wing.

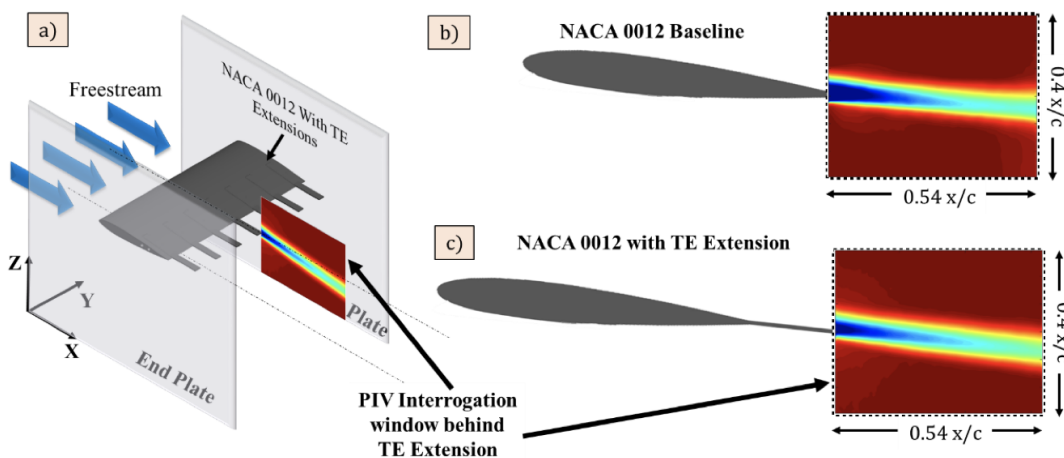


**Figure 7.** a) Schematic of the PIV test setup for the NACA 0012 wing with TE extensions. Similar setup is used for the baseline wing. The PIV interrogation window for (b) the baseline case was located at the TE and (c) for the wing with TE extension, it was location at the trailing edge of TE

### 166 3. Results

#### 167 3.1. Force-Based Experimental Results

168 The coefficient of lift variation with angle of attack is shown in Figure 8 for the Reynolds number  
 169 of 200,000 for both the baseline case and the wing with TE extensions. The coefficient of lift variation is  
 170 compared with the theoretical lift coefficient variation given by McCormick's formula (McCormick  
 171 [15]). According to McCormick's formula, the lift curve slope depends on the aspect ratio by,

$$a = \frac{dC_L}{d\alpha} = a_0 \left( \frac{AR}{AR + 2(\frac{AR+4}{AR+2})} \right) \quad (1)$$

172 where  $a_0 = 2\pi$ , according to thin airfoil theory. The best fit line of the lift curve gives an effective  
 173 aspect ratio of 2 which is smaller than the intended aspect ratio of 4. The reduction in effective aspect  
 174 ratio could be due to the wing-splitter plate interface contributing to three dimensionality of the flow.  
 175 The baseline results shows good match with the results from Ngo and Barlow [16] for a Reynolds  
 176 number of 480,000 for AR 2. The added 11% surface area was taken into account in the calculation of  
 177 lift from the wing with the TE extensions case. The comparison of lift coefficient magnitude between  
 178 the baseline and the wing with TE extensions shows almost no variations as a function of angle of

179 attack. Any changes in lift coefficient falls between the uncertainty band of the sensor as indicated by  
 180 the error bars.

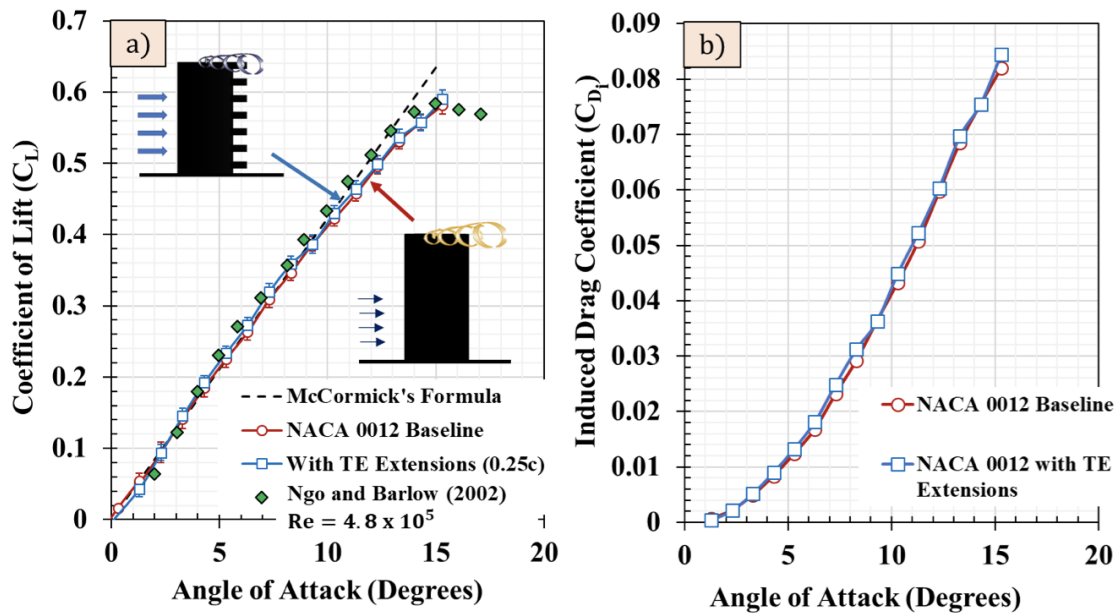


Figure 8. a) Variation of Coefficient of Lift with angle of attack for baseline wing and wing with TE extensions. The lift curve slope shows similar variation with negligible differences between the two cases. b) Variation of coefficient of induced drag for both cases.

181 The differences in lift is used to calculate the differences in the induced drag. The induced drag  
 182 was found by,

$$C_{D\text{ Induced}} = \frac{C_L^2}{\pi e AR} \quad (2)$$

183 where  $e = 0$  is the span efficiency and  $AR$  is the aspect ratio. The span efficiency of the baseline and  
 184 the 11-hole wing was found using the lift curve slope equation from thin airfoil theory (Equation 3).

$$a = \frac{a_0}{1 + \frac{a_0}{\pi e AR}} \quad (3)$$

185 where  $a$  is the lift curve slope of the finite wing and  $a_0 = 2\pi$ . From Equation 6, the span efficiency  
 186 for the baseline was 0.69 for both the cases since they have the same lift curve slope. The wing with  
 187 TE extensions shows higher induced drag coefficient across all angles of attack (Figure 8b). At 14  
 188 angle of attack, the induced drag shows a 6% increase in the wing with TE extensions when compared  
 189 to the baseline. At lower angles of attack, the differences in the induced drag between two cases is  
 190 not resolvable due to the uncertainty limit of the ATI mini-40 sensor. Because drag is an order of  
 191 magnitude less than the lift, the sensor was not capable of measuring the differences in the drag forces  
 192 between the two cases. Therefore, streamwise Particle Image Velocimetry (PIV) was used to determine  
 193 the momentum deficit and the parasitic drag of the wing configurations. The results from the PIV are  
 194 discussed in the section below.

### 195 3.2. Momentum Deficit

196 The streamwise velocity  $U_X$  contour obtained behind the TE extension and behind the trailing  
 197 edge of the baseline wing is shown in Figure 9a. The momentum deficit increases with increase in angle of attack as expected for the both cases. However, subtle differences can be observed in the  
 198

199 momentum deficit between the two cases. At a  $2^\circ$  angle of attack, the momentum deficit behind the  
 200 TE extension is greater than the momentum deficit behind the trailing edge of the wing. This could  
 201 be due to increased skin friction drag due to the presence of the TE extension. As the angle of attack  
 202 increases, the different trend is observed. At  $4^\circ$  and  $6^\circ$  angle of attack cases, the differences between the  
 203 two cases are hard to observe since the contours look almost similar. However, at  $8^\circ$  angle of attack,  
 204 lower momentum deficit can be observed behind the TE extension when compared to the baseline.  
 205 This shows that the TE extension reduced the pressure drag of the wing.

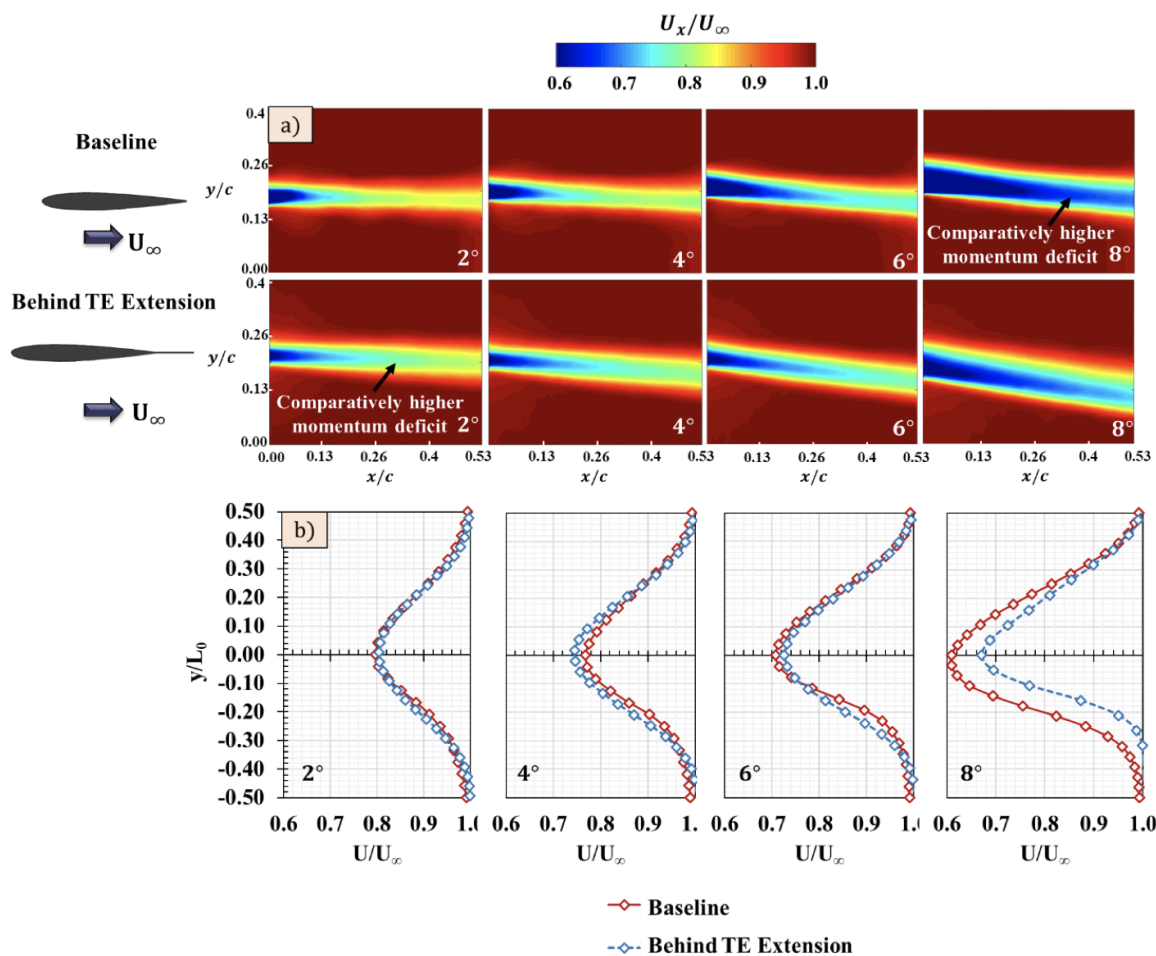


**Figure 9.** a) Streamwise velocity contours in FSL behind the trailing edge of the NACA 0012 wing and behind the TE extension b) Momentum deficit profiles at different angles of attack for both cases. The momentum deficit behind the TE extension is lower at higher angles of attack when compared to the baseline.

206 These observations are more apparent in the momentum deficit profiles shown in Figure 9b. The  
 207 profiles were taken by averaging 10 data columns in the center of the field of view. The normalized  
 208 streamwise velocity is plotted against the normalized wake-half width  $y/L_0$  where  $L_0$  is the wake  
 209 half-width which is considered as the location of 99%  $U_\infty$ . The profiles indicate that the momentum  
 210 deficit at  $2^\circ$  and  $4^\circ$  angles of attack between the two cases are similar. At  $6^\circ$  and  $8^\circ$  angle of attack  
 211 however, clear differences between the two cases can be seen. The momentum deficit behind the  
 212 TE extension is clearly lower than the baseline. The momentum deficit profiles shown in Figure 9b  
 213 was used to determine the total parasitic drag coefficient of the baseline NACA 0012 wing and the  
 214 wing with TE extensions. The total parasitic drag coefficient of the wing was found by integrating the

215 sectional drag coefficient along wingspan. The sectional drag coefficient behind the trailing edge and  
216 the TE extension was determined by the momentum deficit equation,

$$C_D = \frac{\rho U_\infty^2}{q_\infty S} \int \frac{U_x}{U_\infty} \left(1 - \frac{U_x}{U_\infty}\right) dy \quad (4)$$

217 The drag coefficient variation with angle of attack is shown in Figure 10. As expected, the drag  
218 coefficient behind the trailing edge varies non-linearly with the angle of attack for both cases. The  
219 magnitude of the drag coefficient behind the TE extension is lower than the baseline at all angles of  
220 attack. Even though the momentum deficit profiles in Figure 9b look similar for both the cases at lower  
221 angles of attack, the TE extension case has a higher chord length and surface area when compared to  
222 the baseline case. Therefore, for a similar normalized momentum deficit profile, the coefficient of drag  
223 is lower in the wake behind the TE extension.

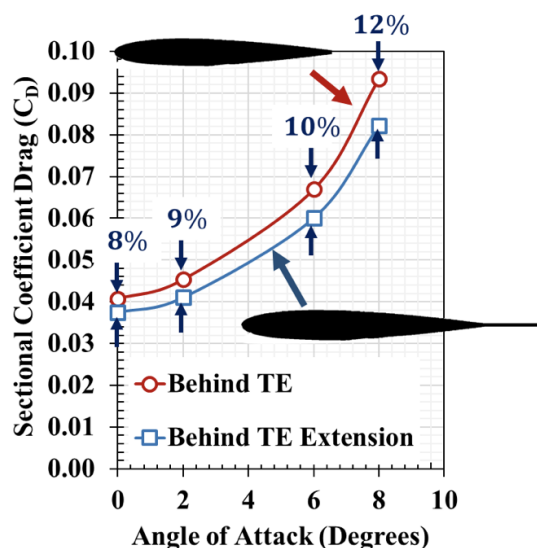
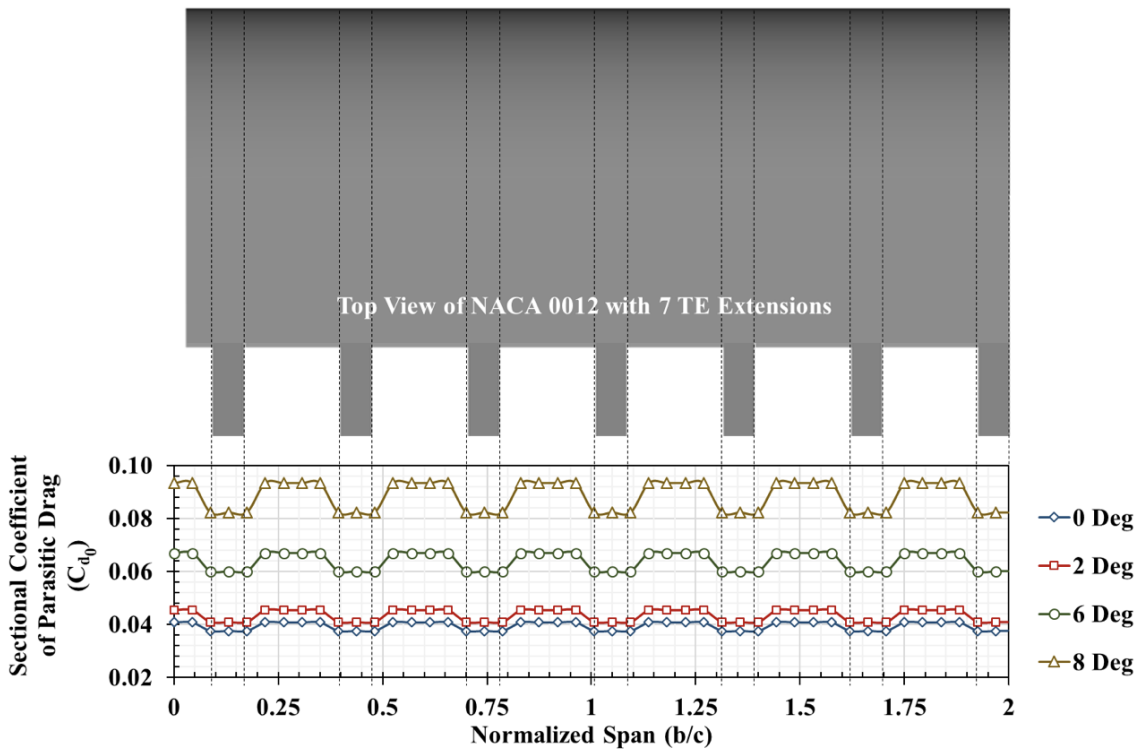


Figure 10. Variation of coefficient drag estimation behind the trailing edge and behind TE extension a function of angle of attack. The estimated drag coefficient behind the TE extension is lower than the drag coefficient behind the hole.

224 The differences in the sectional coefficient of drag increases with increase in angle of attack from  
225 8% at 2° to 12% at 8°. To determine the total parasitic drag coefficient of the entire wing with and  
226 without TE extensions, a theoretical distribution of the sectional drag coefficient is plotted in Figure 11  
227 for 8-hole wing using the drag coefficient values obtained from the momentum integral. The sections  
228 of the wing with the TE extension has a lower drag coefficient than trailing edge as observed in Figure  
229 10. The theoretical drag coefficient distribution increases with angle of attack as expected.

230 The total drag coefficient of the wing was found by integrating the sectional drag coefficient along  
231 the span of the wing. The net parasitic drag coefficient of the NACA 0012 baseline wing and the wing  
232 with TE extensions are shown in Figure 12a for multiple angles of attack. The total parasite drag of  
233 the wing with TE extensions is lower than the NACA 0012 baseline wing across all angles of attack.  
234 Adding the induced drag found from force based experiment and parasitic drag data found from PIV,  
235 the total drag coefficient for the baseline and the wing with TE extension is shown in Figure 12b. The  
236 total drag for the wing with TE extensions is also lower when compared to the baseline at all angles of  
237 attack. Since the induced drag remained the same for both the cases (Figure 8b), the total drag shows  
238 the same trend as the parasite drag coefficient. Total drag reduction in the order of 8% is observed at  
239 an angle of attack of 0° increasing to 9% at 8° angle of attack. The average reduction in drag coefficient

<sup>240</sup> due to the TE extensions is around 8%. This result indicates that the TE extensions are effective at all  
<sup>241</sup> angles of attack.



**Figure 11.** Section drag coefficient variation across the span for wing with seven TE extensions. The drag coefficient behind the TE extension is lower than the drag coefficient behind the trailing edge of NACA 0012.

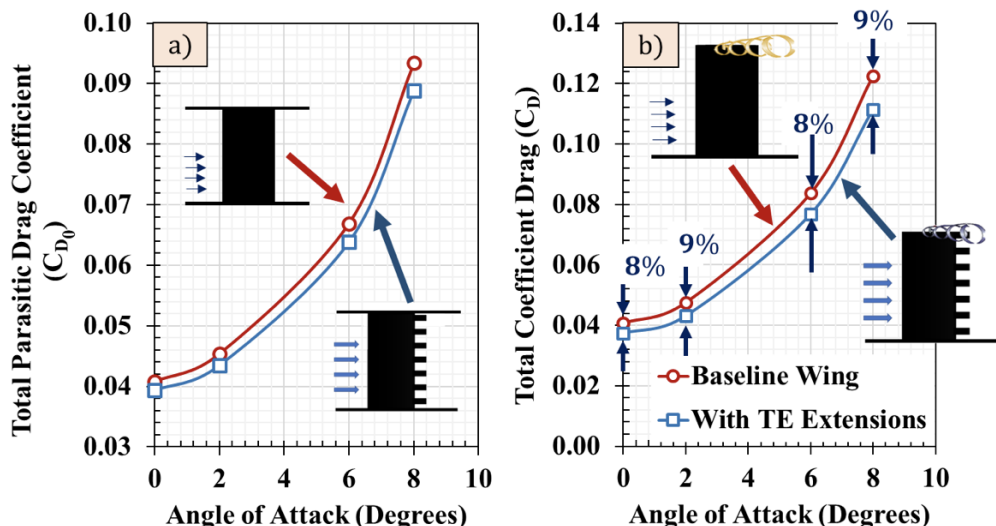


**Figure 12.** Variation of a) net parasitic drag coefficient and b) total drag coefficient of the baseline wing and wing with TE extensions. The wing with TE extensions show an average decrease in drag coefficient around 8%.

## 242 3.3. Y-Vorticity

243 The vorticity contours and profiles behind the wake of the baseline NACA 0012 wing and with  
 244 the TE extensions can be seen in Figure 13a and 13b. The Y-vorticity in the wake was determined by

$$\omega_y = \left( \frac{\partial w}{\partial x} - \frac{\partial u}{\partial z} \right) \quad (5)$$

245 The velocity gradients in Equation 8 were determined by central difference technique using the  
 246 experimental velocity data.

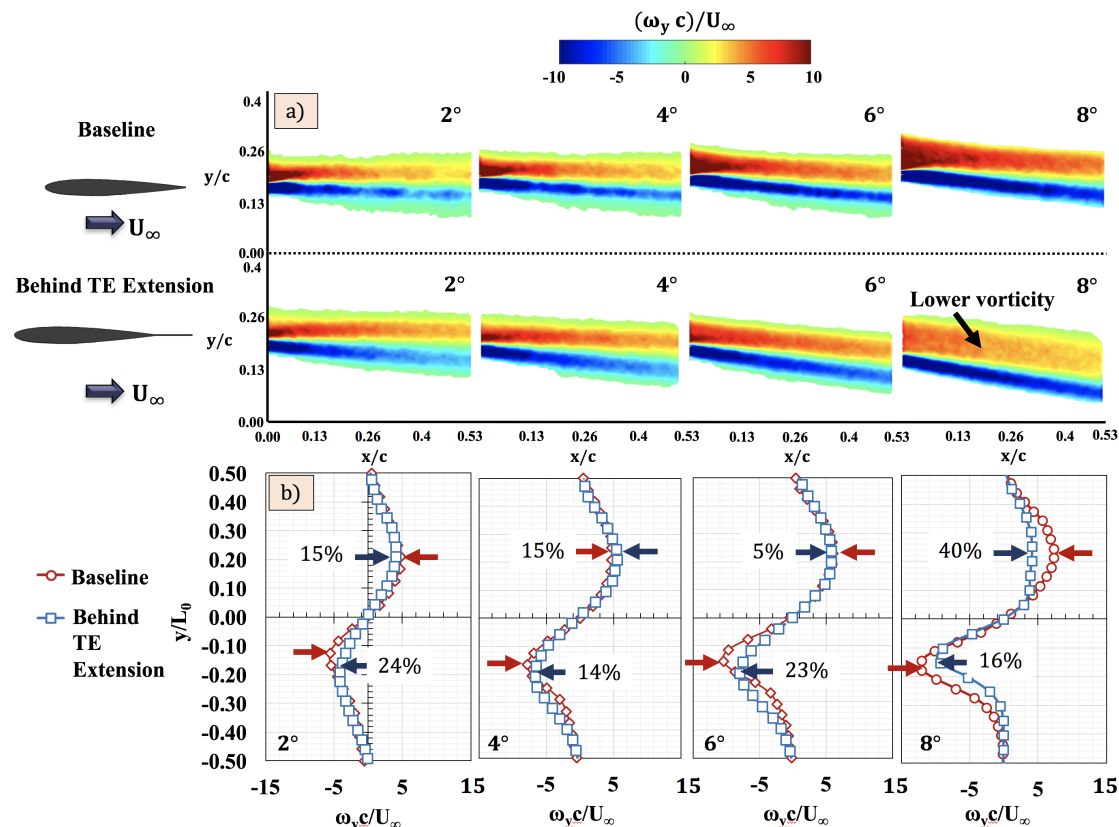


Figure 13. a) Streamwise vorticity contours in FSL behind the trailing edge of the NACA 0012 wing and behind the TE extension b) Vorticity profiles at different angles of attack for both cases. The local rotating velocity behind the TE extension is lower at higher and lower angles of attack when compared to the baseline.

247 Similar magnitudes between the two cases is observed in the vorticity contours at lower angles of  
 248 attack. However, at 8°angle of attack, higher vorticity magnitude is observed behind the TE extension.  
 249 The vorticity profiles across the contours are compared between the two cases in Figure 13b. At a  
 250 2°angle of attack a reduction in vorticity of 15% on the top surface and 24% on the bottom surface was  
 251 observed with TE extensions. Then at 4°angle of attack, the difference in peak vorticity decreased.  
 252 The top surface vorticity had a 15% increase and the bottom had a 14% decrease with TE extensions.  
 253 However, at 8 angle of attack, the extensions reduce the peak vorticity strength by 40% in the top  
 254 surface and 16% on the bottom. This shows that the TE extensions are most effective at higher angles  
 255 of attack as the pressure drag begins to dominate over skin friction drag. The reduced vorticity at  
 256 8 angle of attack also indicates changes in the vortex shedding frequency and magnitude which is  
 257 discussed in the next section. The reduction in vorticity also indicates a reduction in total pressure loss  
 258 through Crocco's theorem which in turn reduces drag.

## 259 3.4. Coherent Structures

260 As seen in the literature review section, vortex shedding frequency and turbulent length scales  
 261 contributes to turbulence-induced pressure fluctuations, sound generation and structural vibrations.  
 262 The effect of the TE extensions on vortex shedding frequency and turbulent length scales can be  
 263 determined by comparing the changes in the coherent structures present in the wake between the  
 264 baseline wing and wing with TE extensions. The coherent structures can be determined by performing  
 265 two-point correlation of fluctuating velocities ( $u'$  and  $v'$ ) in the wake. The two-point correlation also  
 266 allows to determine the length scales associated with the coherent turbulent motions. Bendat and  
 267 Piersol [17] defined the two-point correlation as

$$\rho_{u_i u_j} = \frac{u'_i(X_1, t) * u'_j(X_2, t + \tau)}{\sqrt{u'_i(X_1)^2} \sqrt{u'_j(X_2)^2}} \quad (6)$$

268 where  $X_1$  and  $X_2$  are two spatial locations in the PIV field of view,  $\tau$  is the time delay (which is chosen  
 269 to be zero for the results shown below),  $u'$  represents the fluctuating velocities in  $i$  and  $j$  direction.  
 270 Figure 14 and Figure 15 show the contour levels of the normalized two-point correlation functions  
 271 with zero time delay of the streamwise ( $u$ ) and transverse ( $v$ ) fluctuating velocities respectively for 2°,  
 272 4°, 6°, and 8° angles of attack in the wake of the baseline wing and in the wake of the TE extension. In  
 273 each case, the reference point ( $X_1$ ) is chosen to be at the center of the upper shear layer as indicated in  
 274 Figure 14.

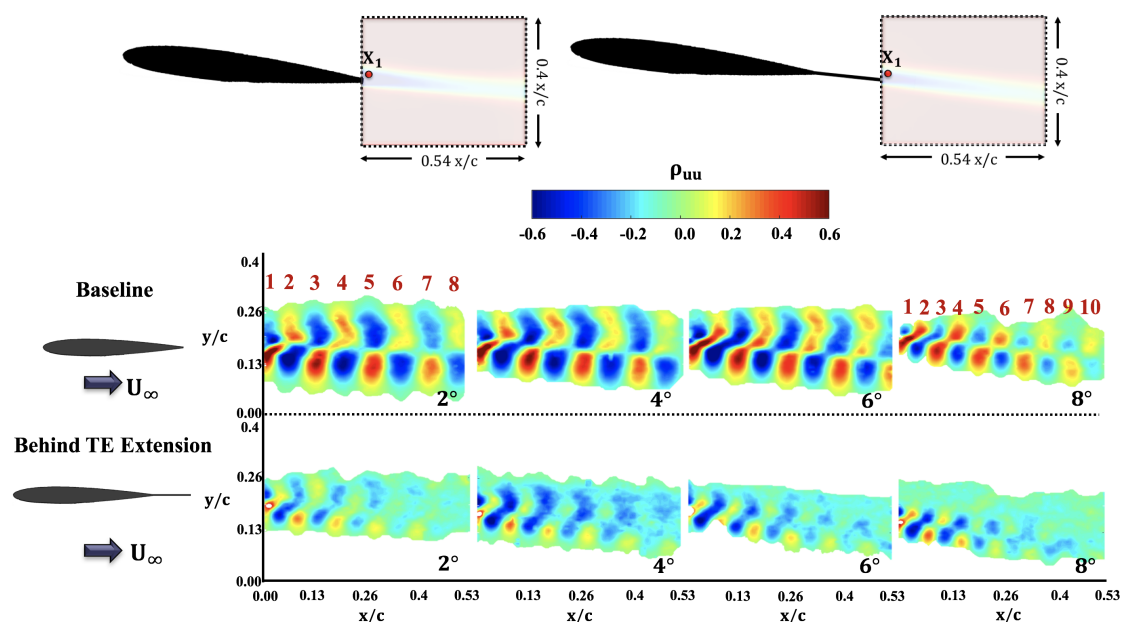
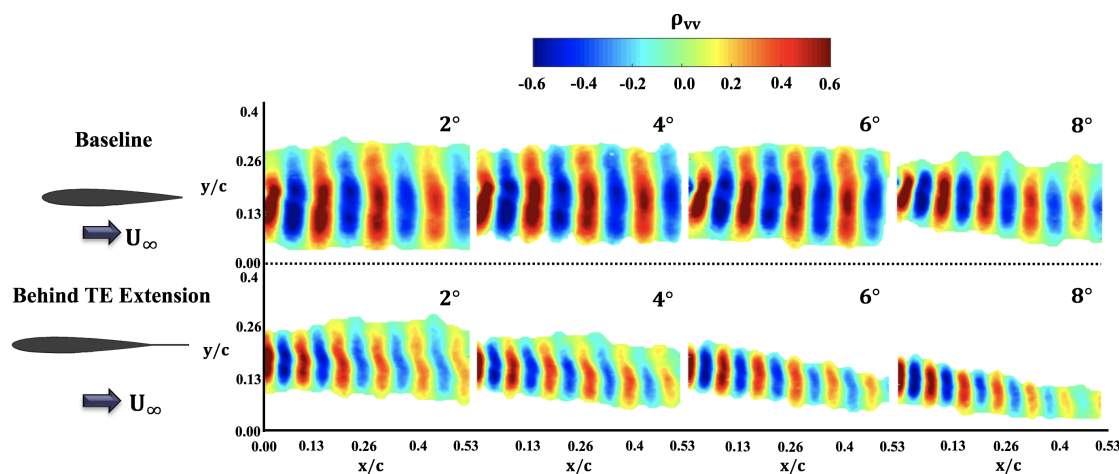


Figure 14. Contours of two-point correlation of the streamwise velocity component for the baseline wing and for the wing with TE extensions. Weaker correlations are observed in the wake behind the TE extension indicating lower length scales and velocity fluctuations.

275 The intent behind the correlation is to highlight the correlation in velocity fluctuations between  
 276 the upper surface boundary layer and the near wake. The  $\rho_{u_i u_j}$  contour images for the baseline case  
 277 shows extensive coherent structures of alternating positive and negative correlation values. Specifically,  
 278 spatially alternating regions of positive and negative correlation are indicative of the spatially and  
 279 temporally periodic motions of the fluid. These motions can be related to the tonal character of  
 280 fluctuations in the flowfield at the frequency of vortex shedding. In the baseline case, the coherent  
 281 structures are well formed in the shear layer emanating from the lower surface of the wing. The

282 magnitude of correlations is also higher when compared to the upper surface shear layer. As the  
 283 angle of attack increases, the length scales (represented by the horizontal distance of each coherent  
 284 structure) decreases due to increased vortex shedding frequency. This can be observed by quantifying  
 285 the number of coherent structures in the wake. At 2°angle of attack, there are eight coherent structure  
 286 and at 8°angle of attack, there are ten coherent structures. However, in the wake of TE extension, the  
 287 correlation of the upper surface shear layer and the near wake is significantly lower when compared to  
 288 the baseline case. This indicates a comparatively weaker vortex shedding and turbulent fluctuations in  
 289 the wake of the TE extension. It is interesting to note that with the increase in the downstream distance,  
 290 the correlation of the velocity fluctuations in the TE extension case almost goes to zero at all angles of  
 291 attack. However, in the baseline case, there is a strong correlation across the field of view.



**Figure 15.** Contours of two-point correlation of the transverse velocity component for the baseline wing and for the wing with TE extensions. Similar to  $\rho_{u_i u_j}$ , weaker correlations are observed in the wake behind the TE extension lower velocity fluctuations. Also, the decrease in wavelength of the correlation indicates a decrease in turbulent length scales.

292 Similar behavior is observed in the  $\rho_{vv}$  (transverse) velocity correlations in the wake of the baseline  
 293 wing and in the wake of the TE extension. The large alternating regions of positive and negative  
 294 correlation appear in the baseline and the TE extension cases but the wavelength of the correlations in  
 295 the TE extension is almost of half of that of the baseline wing. The reduction in length scales indicate  
 296 lower velocity fluctuations in the wake of the TE extension which results in lower pressure fluctuations  
 297 and lower drag as observed in Figure 12b. The decrease in turbulent length scales decreases the inertial  
 298 subrange of the energy spectrum and increases the viscous dissipation which results in lower drag  
 299 coefficient of the wing. The reduced fluctuations in the TE extension case can also be seen in the RMS  
 300 quantities of the streamwise and transverse velocities.

### 301 3.5. Reynolds Stress

302 The Reynolds stress components are indicative of the turbulent intensity within a developing  
 303 shear layer. Mohsen [18] suggested that the local maximum Reynolds stress  $(u'v')_{max}$  in the Reynolds  
 304 stress profile may be correlated to the large pressure fluctuations. Therefore, the Reynolds stress  
 305 distribution in the wake are of great interest as they can indicate how TE extensions affect the amount  
 306 of turbulence in the flow. The contour plots and profiles of the Reynolds stress comparing the NACA  
 307 0012 baseline wing and with TE extensions can be seen in Figure 16a and 16b.

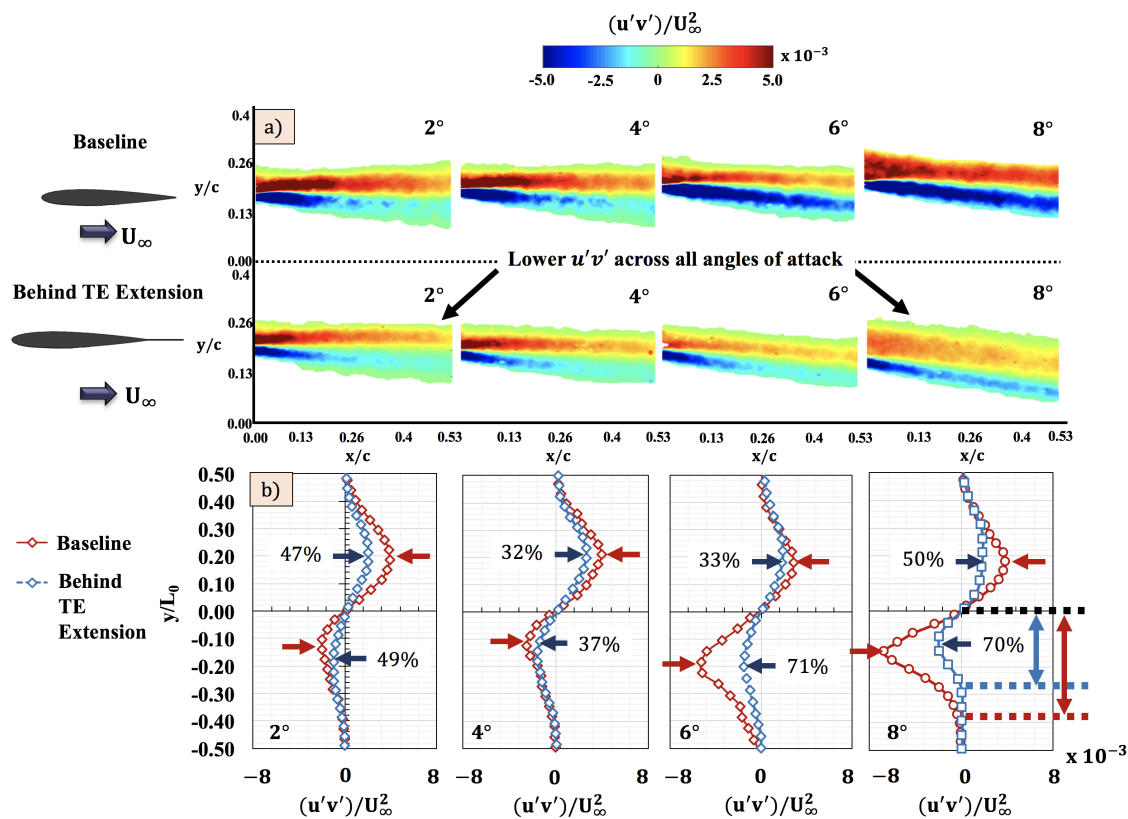


**Figure 16.** a) Streamwise Reynolds stress contours in FSL behind the trailing edge of the NACA 0012 wing and behind the TE extension b) Reynolds stress profiles at different angles of attack for both cases. The Reynolds stress behind the TE extension is lower across all angles of attack when compared to the baseline.

The magnitude of the both the upper and lower surface Reynolds stress behind the TE extension is lower than the baseline case at all angles of attack. The lower magnitude behind the TE extension indicates that the turbulent fluctuations emanating from the upper and lower surface boundary layer has reduced drastically when compared to the baseline. In both the cases, the Reynolds stress varies in the streamwise direction. But the changes in the streamwise direction in the Reynolds stress is greater in the baseline case when compared to the TE extension case. This trend can be clearly seen at 8° angle of attack. A uniform variation in the Reynolds stress can be observed behind the extended TE case where the Reynolds stress decreases with increase in downstream distance behind the trailing edge of the baseline wing. The differences in the Reynolds stress between the two cases can be seen clearly in the profiles shown in Figure 16b. Surprisingly, the magnitude of the Reynolds stress in the upper surface is lower than the magnitude of the Reynolds stress in the lower surface in both cases. But the magnitude of the Reynolds stress in both the upper and lower surface of the TE extension case is lower than the baseline in all angles of attack. The Reynolds stress is lowered by 47% and 49% on the upper and lower surfaces respectively at 2° with the TE extensions. The peak Reynolds stress differences then decreases to 32% and 37% at 4° angle of attack with extensions and again greatly increase at higher angles of attack. This displays a trend similar to the vorticity profiles. At 8° the peak Reynolds stress with the TE extensions is 50% lower on the upper surface and 70% on the lower surfaces. It is interesting to note that the TE extension affect the Reynolds stress in the lower surface significantly than the upper surface.

### 3.6. Root-Mean Square (RMS) Velocities

The root mean square of U and Y velocities were determined by

$$U_{RMS} = \sqrt{(u'_x)^2} \quad (7)$$

$$V_{RMS} = \sqrt{(v'_y)^2} \quad (8)$$

329 where  $u'_x$  is the fluctuating velocity about the x-axis,  $u'_y$  is the fluctuating velocity about the y-axis.  
 330 The freestream normalized  $U_{RMS}$  is shown in Figure 17 for both the baseline and the wing with TE  
 331 extension. The magnitude of  $U_{RMS}$  increases with increase in angle of attack for both cases but in all  
 332 the angles of attack, the magnitude of the RMS is greater in the wake behind the baseline wing when  
 333 compared to the TE extension. Therefore, the fluctuations in the  $U$  velocity are reduced significantly  
 334 by the TE extension.

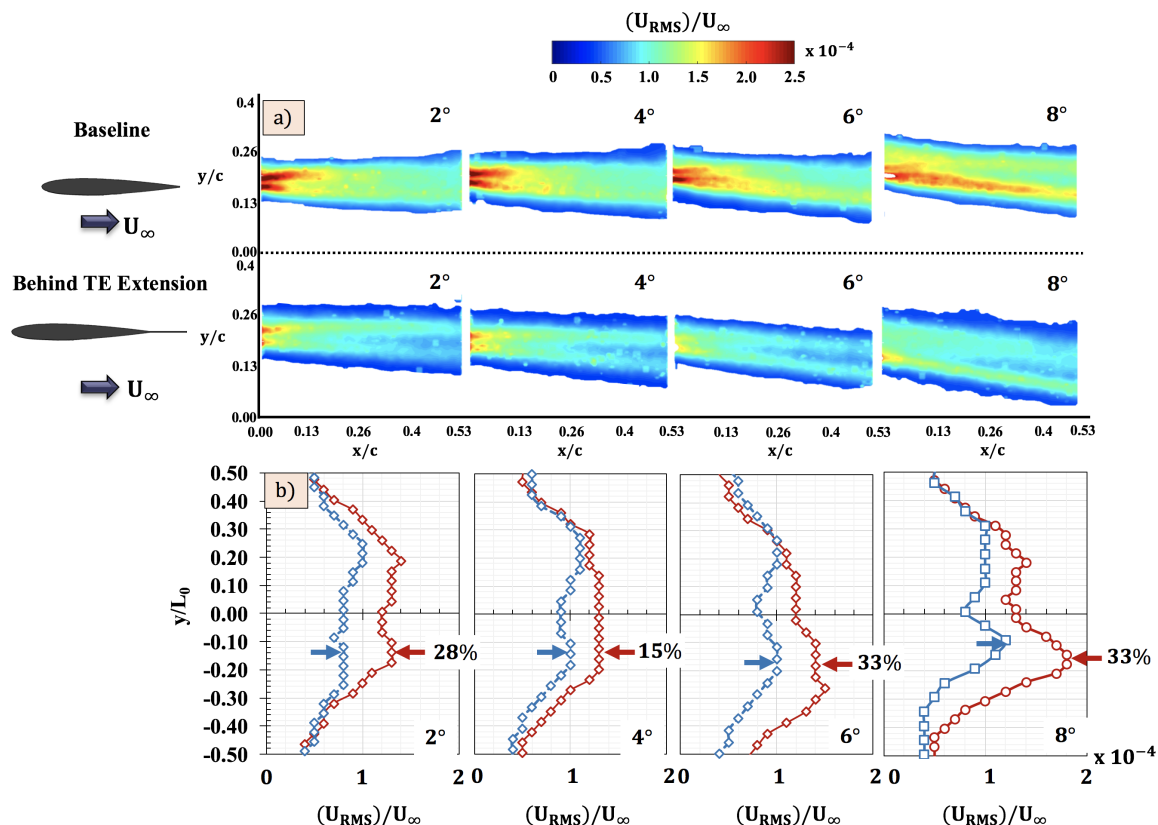
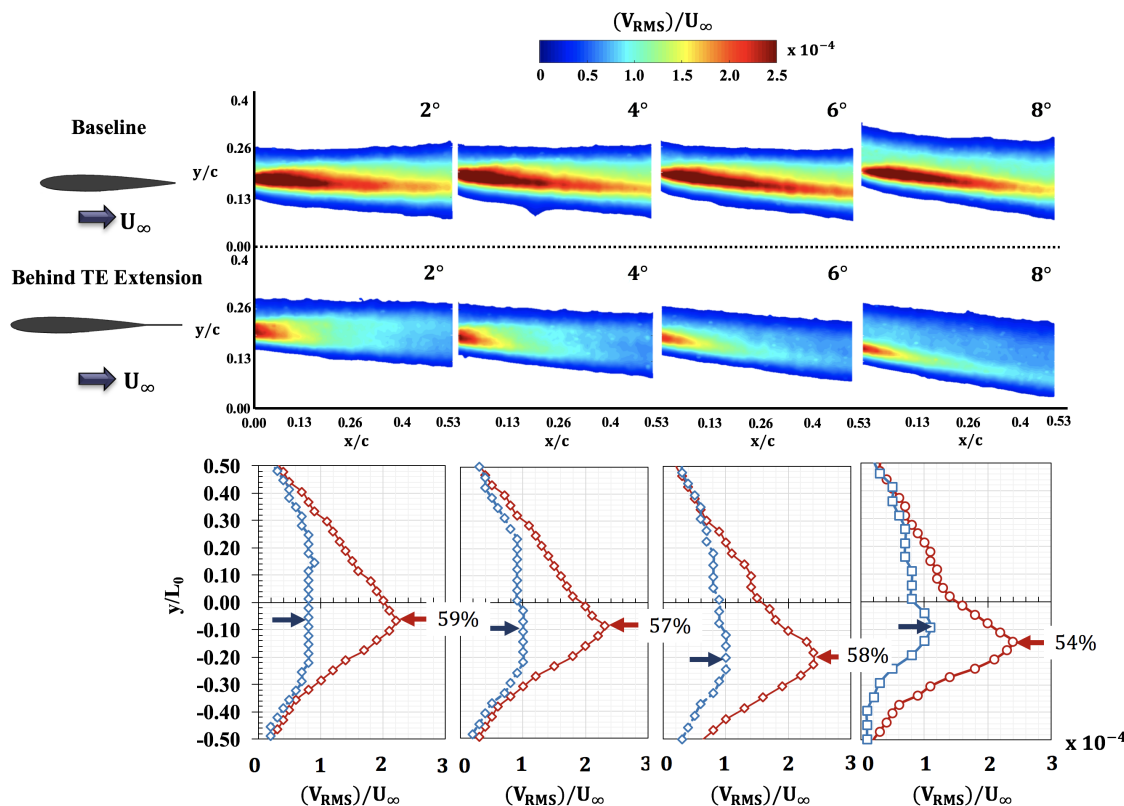


Figure 17. a) Streamwise  $U_{RMS}$  contours in FSL behind the trailing edge of the NACA 0012 wing and behind the TE extension. b)  $U_{RMS}$  profiles at different angles of attack for both cases. Large decreases were observed in the  $U_{RMS}$  of the TE extension.

335 In both cases and in all angles of attack, the  $U_{RMS}$  in the lower surface was found to be greater  
 336 than the upper surface. This result correlates with the increase Reynolds stress in the lower surface  
 337 when compared to the upper surface of the wing. The differences in the  $U_{RMS}$  can be seen clearly in  
 338 the URMS profiles shown in Figure 17b. The average difference in the peak  $U_{RMS}$  behind the baseline  
 339 wing and behind the TE extension is around 30%. Similar results are observed in  $V_{RMS}$  as well which  
 340 is shown in Figure 18a. The normalized  $V_{RMS}$  values of  $1.8 \times 10^{-5}$  and  $2.0 \times 10^{-5}$  are highlighted in  
 341 white to distinctly observe the free shear layer. Similar to the  $U_{RMS}$ , the magnitude of the  $V_{RMS}$  in  
 342 the wake behind the TE extension is significantly reduced. The differences can also be clearly seen  
 343 in the  $V_{RMS}$  profiles shown in Figure 18b. The peak differences in  $V_{RMS}$  profiles display consistent  
 344 reductions with TE extensions at an average of 57%. The magnitude decrease in  $V_{RMS}$  is greater than  
 345 the magnitude decrease in  $U_{RMS}$  in the wake behind the TE extension. Similar trend was seen in the

346 coherent structures. The two-point correlation of the transverse velocity showed significant changes  
 347 when compared to the streamwise velocity correlation. The reduction in the length scales might be the  
 348 cause of lower fluctuations in the wake behind the TE extension.



**Figure 18.** a) Streamwise  $V_{RMS}$  contours in FSL behind the trailing edge of the NACA 0012 wing and behind the TE extension b)  $V_{RMS}$  profiles at different angles of attack for both cases. Large decreases where observed in the  $V_{RMS}$  of the TE extension.

#### 349 4. Conclusions

350 A NACA 0012 baseline semi-span wing model was tested with and without segmented trailing  
 351 edge (TE) extensions. Force and PIV experiments were conducted to analyze how the segmented TE  
 352 extensions affected the vorticity and turbulent signatures in the wake. The prominent conclusions  
 353 taken from the research are:

- 354 1. The TE extensions had minor effect on the coefficient of lift but had measurable impact on the  
 355 coefficient of drag at high angles of attack. With the segmented TE extensions, the total drag  
 356 coefficient reduced by 8% at 8° angle of attack.
- 357 2. Evidence for the cause of reduction in parasitic drag with TE extensions was supported by  
 358 mean flow quantities such as mean velocity and normalized vorticity. Both parameters showed  
 359 measurable and significant reductions when compared to the baseline especially in the vorticity  
 360 case. The average reduction in vorticity is in the order of 40% at 8° angle of attack.
- 361 3. The reduction in vorticity behind TE extension was further supported by determining the  
 362 coherent structures in the wake. The TE extensions reduced the length scales and the correlation  
 363 of the wake and the upper surface boundary layer which indicates lower velocity and pressure  
 364 fluctuations.
- 365 4. The lower pressure fluctuations can be supported by the changes observed in the Reynolds  
 366 stress. On an average, the magnitude of the Reynolds stress was reduced by 40% on the upper  
 367 surface and by 55% on the lower surface.

368 5. The reduction in fluctuations are further validated by determining  $U_{RMS}$  and  $V_{RMS}$  which  
369 showed an average decrease in the magnitude by 15% and 57% respectively.

370 These results provide evidence to consider segmented trailing edge extensions as a means to  
371 reduce turbulent fluctuations and vortex shedding in the wake of the wing without compromising on  
372 the lift production.

373 **Conflicts of Interest:** The authors declare no conflict of interest.

374

375 1. Theodorsen, T.; Stickle, G.W. *Effect of a Trailing-edge Extension on the Characteristics of a Propeller Section*;  
376 National Advisory Committee for Aeronautics, 1944.

377 2. Ito, A. The effect of trailing edge extensions on the performance of the Göttingen 797 and the Wortmann  
378 FX 63-137 aerofoil sections at Reynolds numbers between  $3 \times 10^5$  and  $1 \times 10^6$ . *The Aeronautical Journal* **1989**,  
379 93, 283–289.

380 3. Yarusevych, S.; Sullivan, P.E.; Kawall, J.G. On vortex shedding from an airfoil in low-Reynolds-number  
381 flows. *Journal of Fluid Mechanics* **2009**, 632, 245–271.

382 4. Huang, R.F.; Lin, C.L. Vortex shedding and shear-layer instability of wing at low-Reynolds numbers. *AIAA  
383 journal* **1995**, 33, 1398–1403.

384 5. Huang, R.F.; Lee, H.W. Turbulence effect on frequency characteristics of unsteady motions in wake of wing.  
385 *AIAA journal* **2000**, 38, 87–94.

386 6. Guan, Y.; Pröbsting, S.; Stephens, D.; Gupta, A.; Morris, S.C. On the wake flow of asymmetrically beveled  
387 trailing edges. *Experiments in Fluids* **2016**, 57, 78.

388 7. Butler, S. Aircraft drag prediction for project appraisal and performance estimation. *AGARD Aerodyn.  
389 Drag 50 p(SEE N 74-14709 06-01)* **1973**.

390 8. Stanewsky, E. Adaptive wing and flow control technology. *Progress in Aerospace Sciences* **2001**, 37, 583–667.

391 9. Neuhart, D.H.; Pendergraft Jr, O.C. A water tunnel study of Gurney flaps **1988**.

392 10. Jang, C.S.; Ross, J.C.; Cummings, R.M. Numerical investigation of an airfoil with a Gurney flap. *Aircraft  
393 Design* **1998**, 1, 75.

394 11. Storms, B.L.; Jang, C.S. Lift enhancement of an airfoil using a Gurney flap and vortex generators. *Journal of  
395 Aircraft* **1994**, 31, 542–547.

396 12. Traub, L.W. Examination of Gurney Flap Pressure and Shedding Characteristics. *Journal of Aircraft* **2017**,  
397 54, 1990–1995.

398 13. Liu, T.; Montefort, J.; Liou, W.; Pantula, S.; Shams, Q. Lift enhancement by static extended trailing edge.  
399 *Journal of Aircraft* **2007**, 44, 1939–1947.

400 14. Lee, H.T.; Kroo, I.; Bieniawski, S. Flutter suppression for high aspect ratio flexible wings using microflaps.  
401 43rd AIAA/ASME/ASCE/AHS/ASC Structures, Structural Dynamics, and Materials Conference, 2002, p.  
402 1717.

403 15. McCormick, B.W. *Aerodynamics, aeronautics, and flight mechanics*; Vol. 2, Wiley New York, 1995.

404 16. Ngo, H.T.; Barlow, L.E. Lifting surface with active variable tip member and method for influencing lifting  
405 surface behavior therewith, 2002. US Patent 6,394,397.

406 17. Bendat, J.S.; Piersol, A.G. Random data analysis and measurement procedures, 2000.

407 18. Mohsen, A.M. Experimental investigation of the wall pressure fluctuations in subsonic separated flows.  
408 Technical report, BOEING COMMERCIAL AIRPLANE CO RENTON WA, 1967.